NANO LETTERS

pubs.acs.org/NanoLett

Letter

A High Aspect Ratio Inverse-Designed Holey Metalens

Soon Wei Daniel Lim,*[,†] Maryna L. Meretska,[†] and Federico Capasso*

Cite This: *Nano Lett.* 2021, 21, 8642−8649

Read Online

ACCESS | Metrics & More | Article Recommendations | Supporting Information

ABSTRACT: Free-standing nanofins or pillar meta-atoms are the most common constituent building blocks in metalenses and metasurfaces in general. Here, we present an alternative metasurface geometry based on high aspect ratio via-holes. We design and characterize metalenses comprising ultradeep via-holes in 5 μm thick free-standing silicon membranes with hole aspect ratios approaching 30:1. These metalenses focus incident infrared light into a diffraction-limited spot. Instead of shaping the metasurface optical phase profile alone, we engineer both transmitted phase and amplitude profiles simultaneously by inverse-designing the lens effective index profile. This approach improves the impedance match between the incident and transmitted waves, thereby increasing the focusing efficiency. The holey platform increases the accessible aspect ratio of optical nanostructures without sacrificing mechanical robustness. The high nanostructure aspect ratio also increases the chromatic group delay range attainable, paving the way for a generation of high aspect ratio ruggedized flat optics, including large-area broadband achromatic metalenses.

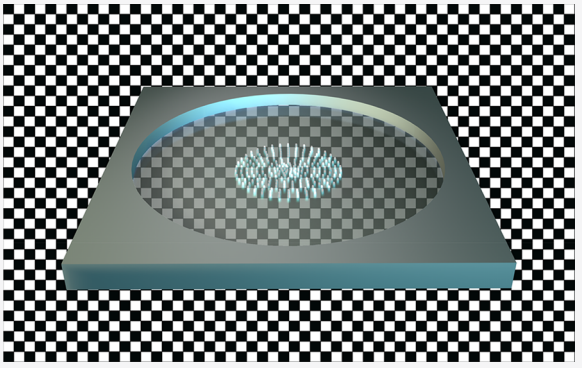

KEYWORDS: *Metalenses, metasurfaces, silicon membrane, high aspect ratio structures, flat optics, infrared optics*

Metasurfaces have attracted much attention due to their multifunctionality and ability to exceed the performance of conventional refractive optics for some applications.[1−4] A centimeter-scale all-glass metalens fabricated using deep-ultraviolet (DUV) lithography exhibited lower monochromatic aberrations than an equivalent aspheric lens,[5] and a single metasurface combined with an image sensor was turned into a polarization camera.[6] The uniformly flat few-layered geometry also simplifies optical alignment.[7] These surfaces are typically designed with subwavelength nanostructures (meta-atoms) that allow the phase, amplitude, and polarization of incident light to be manipulated with precision. Through techniques such as dispersion engineering,[7] the shape of the nanostructures is chosen to produce optical responses that exceed the capabilities of the bulk material. Importantly, the nanostructures can be fabricated using modern complementary metal-oxide-semiconductor (CMOS)-compatible technologies[5,8] and high throughput nanoimprinting methods,[9,10] enabling these devices to be scaled up to high volumes reproducibly.

Early plasmonic metasurfaces used nanoholes or slits in thin sheets of metal as meta-atoms for lensing and other applications.[11−16] The application of these devices was limited by absorptive ohmic losses[17] and the lack of control over the full 2π phase delay for light. The latter arose from the small height-to-width aspect ratio of the fabricated meta-atoms, which was limited to 5:1 for plasmonic lenses.[15] High-refractive index dielectric nanopillars were later proposed as alternative meta-atoms at visible wavelengths.[18,19] These dielectric materials are transparent at the design wavelength and can achieve higher aspect ratio structures (approaching 20:1)[20] compared to plasmonic nanoholes, allowing the fabricated metasurfaces to be efficient and achieve full phase control. There has since been an explosion in applications employing this pillar-based metasurface platform, such as fixed and varifocal metalenses,[21−23] optical traps,[24] polarimeters,[6,25] and generators of vortex beams,[26−29] Bessel-beam and Airy beams,[30−32] singular light,[33] entangled photons,[34] structural color,[35] and holograms.[36−38]

High aspect ratio meta-atoms are desirable in metalens design. On one hand, the characteristic in-plane spacing and size of meta-atoms should be smaller than the design wavelength, as this gives one the ability to engineer the optical wavefront with high spatial precision and suppress higher diffraction orders. On the other hand, the meta-atoms should be tall to maximize the interaction between the incident light and the nanostructured material. Taller meta-atoms expand the range of optical properties that can be tailored for a given range of shapes by expanding the phase control of the incident wavefront and may even allow wavepackets to travel laterally.[39] To obtain full phase coverage and arbitrary structuring of wavefront tilts, meta-atoms must be tall enough to address the

Received: July 4, 2021
Published: October 11, 2021

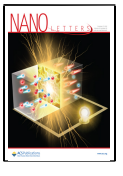

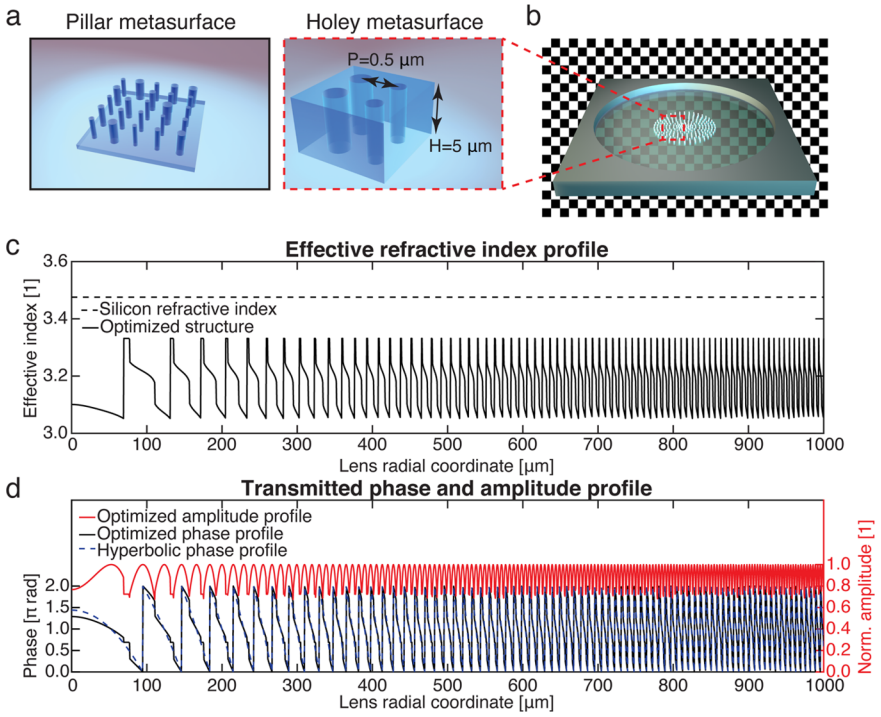

Figure 1. Design of a holey metalens. (a) Comparison between a free-standing pillar metasurface and a holey metasurface. Holey meta-atoms are more stable and robust compared to pillar meta-atoms. (b) Artistic representation of a holey metalens. Monochromatic light with $\lambda = 1.55$ μm is incident on a thin crystalline Si membrane, into which more than 12.5 million via-nanoholes have been etched. The incident optical wavefront is modified by the holey structure and produces a diffraction-limited focal spot. (c) Effective index profile versus the radial coordinate of the metalens obtained by inverse-design optimization. The refractive index of silicon at the design wavelength is indicated with the dashed black line. (d) Plot of the transmitted phase (solid black line) and amplitude (solid red line) profile of optimized structure. A hyperbolic phase profile (dashed blue line) is superimposed for comparison. The transmitted amplitude is normalized to that of the incident plane wave.

entire 2π phase span. Taller meta-atoms also increase the range of group delays that can be achieved, which is essential for engineering the chromatic dispersion of the device and producing achromatic behavior in large scale devices.[40]

However, it is challenging to fabricate high aspect ratio free-standing meta-atoms. Tall pillar/fin-like structures can fall or break during processing (Figure 1a). The maximum aspect ratio routinely used for metasurfaces is 15:1 for titanium dioxide[19] and 20:1 for silicon.[41]

In this paper, we present holey dielectric metasurfaces that achieve high nanostructure aspect ratios and that are mechanically robust. It opens a possible path to achieving large diameter achromatic metalenses by expanding the accessible range of group delays. The metalenses comprise ultradeep via-holes through a thin membrane (Figure 1b) with aspect ratios approaching 30:1. As the material around each hole forms a contiguous structure, the device is inherently robust and can be deployed without a supporting substrate, expanding the application range of this metasurface platform to cases where a substrate cannot be used, such as in ultrafast optics, where a substrate introduces unwanted dispersion.[42]

Flat optics made of nanoholes have been reported previously. The first application of a complementary Babinet-inverted resonator structure to metasurfaces was done by Falcone et al.,[43] drawing inspiration from Babinet's principle of complementarity, which asserts identical diffraction intensity patterns from an opaque body and a hole of identical shape.[44] In dielectric systems, Park et al. used effective index modulation with silicon through-holes for terahertz focusing,[45] Ong et al. performed a numerical study on nanohole arrays for mid-infrared beam deflection,[46] and Wang et al. employed pillars and holes in GaN achromatic metalenses.[47] These studies deployed via-holes with aspect ratios less than 10:1. The meta-atoms used in our metasurface have the potential to achieve even larger aspect ratios beyond the proof-of-concept reported here. Micrometer-sized holes with aspect ratios exceeding 100:1 have been fabricated in silicon micro-electromechanical systems,[48] and nanoporous anodic alumina membranes can achieve aspect ratios larger than 25000:1.[49]

RESULTS

Design. The radial phase profile $\phi(r)$ of a focusing metalens is typically chosen to be a hyperbolic function:

$$\phi(r) = k_0(f - \sqrt{r^2 + f^2}) \quad (1)$$

where $k_0 = 2\pi/\lambda$ is the vacuum wavenumber, f is the focal length, and r is the radial coordinate on the metalens plane, which ranges from 0 to $D/2$, half of the diameter. The hyperbolic phase profile introduces an in-plane phase gradient so that normally incident light is focused a distance f away from the surface, producing a diffraction-limited spot.[1,30,50]

To realize this phase profile, the metasurface is partitioned into pixels of subwavelength spacing. The appropriate meta-atom for each pixel is selected based on its radial position r. These meta-atoms are picked from a library (i.e., a collection) of meta-atoms, where their individual optical responses (e.g., phase, amplitude, polarization) have been simulated in advance through techniques such as finite-difference time-domain simulations or rigorous coupled-wave analysis.

https://doi.org/10.1021/acs.nanolett.1c02612
Nano Lett. 2021, 21, 8642−8649

In this paper, the target phase distribution is realized by use of ultradeep via-holes through a silicon membrane. The acquired phase of each meta-atom pixel is controlled by the diameter of the circular air hole with 2π phase coverage (Supplementary Figure 1a). We define phase relative to that of the incident plane wave just before the lens. The transmission amplitude is strongly dependent on the meta-atom geometry and correlated with the acquired phase, reaching 100% transmission for certain diameters and achieving 0 or π phase shift at these values (Supplementary Figure 1b). Our holey meta-atoms operate in the effective medium regime[51−54] and can be described to a good degree of approximation by the behavior of a dominant Bloch eigenmode with an effective refractive index $n_{\text{eff}}(D)$ (Supplementary Figure 1c) through a slab with thickness H. These effective indices are bounded between the indices of air and silicon. The unity transmission behavior arises due to Fabry−Perot resonances $n_{\text{eff}}k_0H = m\pi$, $m \in 1, 2, 3, \ldots$ of dominant Bloch eigenmode within the slab, at which the reflected waves destructively interfere. A detailed analysis of this behavior, including a comparison between pillar-based and hole-based structures, is provided in Supporting Information section S1.

Conventional focusing metalens design involves engineering only the phase of light, treating the amplitude as constant across the metasurface.[7] This approach is not ideal for meta-atoms with fluctuations of the transmission amplitude since low transmission meta-atoms reduce the overall focusing efficiency. In this study, we use a spatially variant effective refractive index (controlled by the nanohole diameter)[54] under the locally periodic assumption[55,56] as a design parameter. The real-valued effective refractive index captures the behavior of both the amplitude and phase of light upon transmission through a meta-atom and allows one to improve device performance beyond what a consideration of transmission phase alone would achieve.

We choose the optimum effective refractive index distribution in space using automatic differentiation inverse design. The 2 mm diameter metalens is discretized into a series of 2001 thin rings of radial width 0.5 μm. The effective index of each ring is an optimization parameter (Supplementary Figure 2). The objective function to be maximized is the intensity of light at the focus computed using the full vectorial diffraction integral[57] on an automatic differentiation platform,[58,59] which yields the exact objective function gradients for gradient descent optimization. Within the broad family of numerical optimization techniques for nanophotonics,[60] the scheme we employ has a continuous input space (the space of effective indices at each radial position), begins at a good initial solution (specifically, the hyperbolic phase profile), and optimizes the objective function locally. Figure 1c is the plot of an optimal distribution for a metalens with H = 5.3 μm, λ = 1.55 μm, and f = 4 mm using only effective indices attainable by via-holes with 170 nm $\leq D \leq$ 310 nm and pitch P = 500 nm. This hole diameter range was chosen in advance as these holes can be fabricated accurately and reproducibly by our process and has 2π phase coverage, but this choice does not limit the applicability of this optimization method to other diameter ranges. One should note that since the phase varies increasingly quickly with diameter, larger diameter ranges will require higher fabrication precision. Sampling of the highest spatial frequency band at the lens outer edge is well-achieved with P = 500 nm and comprises 12 pixels.

If one holds the transmitted amplitude constant and optimizes only the meta-atom phase using the same process, the optimized phase profile is the hyperbolic one (dashed blue line in Figure 1d). When the effective index is used as the optimization parameter instead (optimization details in Supporting Information section S2), the optimal phase profile deviates from the hyperbolic one and the intensity at the focus is larger than that of phase-only optimization. The optimized phase and amplitude profiles for transmission through the holey metalens mentioned earlier are plotted in Figure 1d as the solid black and red lines, respectively. The optimized profile skips effective indices that have low transmission amplitudes (e.g., those with transmitted phases around $\pi/2$ and $3\pi/2$) in favor of elements with higher transmission amplitudes. This choice increases the focusing efficiency of the resultant metalens beyond that attainable with a hyperbolic profile for the same set of available meta-atoms. For a focusing efficiency defined in terms of the power flux encircled by a 20 μm diameter aperture around the focal spot (2.6× the Airy disk diameter of 7.8 μm), normalized to the incident power, the focusing efficiency of the holey metalens optimized using the effective index method is 67.8%. In comparison, the best hyperbolic phase profile with the same meta-atoms yields an efficiency of 59.6%. The effective index-optimized efficiency is even larger than that of an uncoated bulk silicon plano-convex hyperbolic lens at 64.7%, as calculated using the Fresnel power transmission coefficients at the air/silicon interface $\frac{4(n_{\text{Si}}/n_{\text{air}})}{(n_{\text{Si}}/n_{\text{air}}+1)^2}$ multiplied by the power flux enclosed by the 20 μm diameter aperture of an ideal Airy profile. The large refractive index contrast at λ = 1.55 μm of 1:3.48 produces significant reflective losses.

We studied two systematic fabrication errors that affect the geometry of the entire holey metalens device: deviations of the membrane thickness and hole diameters from their design values. Since well-established semiconductor fabrication techniques can achieve high spatial uniformity with tolerances well below the optical wavelengths, we study systematic fabrication errors that change the geometry of the entire holey metalens instead of less important stochastic variations that are spatially distributed over the same device. We also examine the effect of changing the wavelength of incident light on the focusing properties and efficiency of the holey metalens devices. The results of these systematic perturbations on the focusing properties and efficiency of the holey metalens devices are summarized in Supplementary Figure 3. The focusing quality is preserved under these perturbations, although the device efficiency decreases away from the design parameter values. The fabrication tolerance to remain within half of the peak focusing efficiency is ±64 nm for the membrane thickness and ±16 nm for hole diameters. For chromatic deviations, the spectral range for which the focal spot remains within one depth of focus[61] $\pm\lambda/\{4[1-(1-\text{NA}^2)^{1/2}]\} = \pm 13$ μm of the design focal length in a medium with n = 1 is 1.545 μm to 1.555 μm, where NA is the numerical aperture.

Fabrication. We fabricated monochromatic (λ = 1.55 μm), D = 2 mm, f = 4 mm, NA = 0.24 holey metalenses by patterning an n-doped crystalline silicon-on-insulator (SOI, 5 ± 0.5 μm device layer, 1 μm oxide layer, 500 μm handle layer) wafer and releasing the silicon device layer to create the free-standing silicon membrane. The center-to-center distance of the via-holes is 500 nm on a square lattice, and the highest designed hole aspect ratio is 30:1. The fabrication steps are

https://doi.org/10.1021/acs.nanolett.1c02612
Nano Lett. 2021, 21, 8642−8649

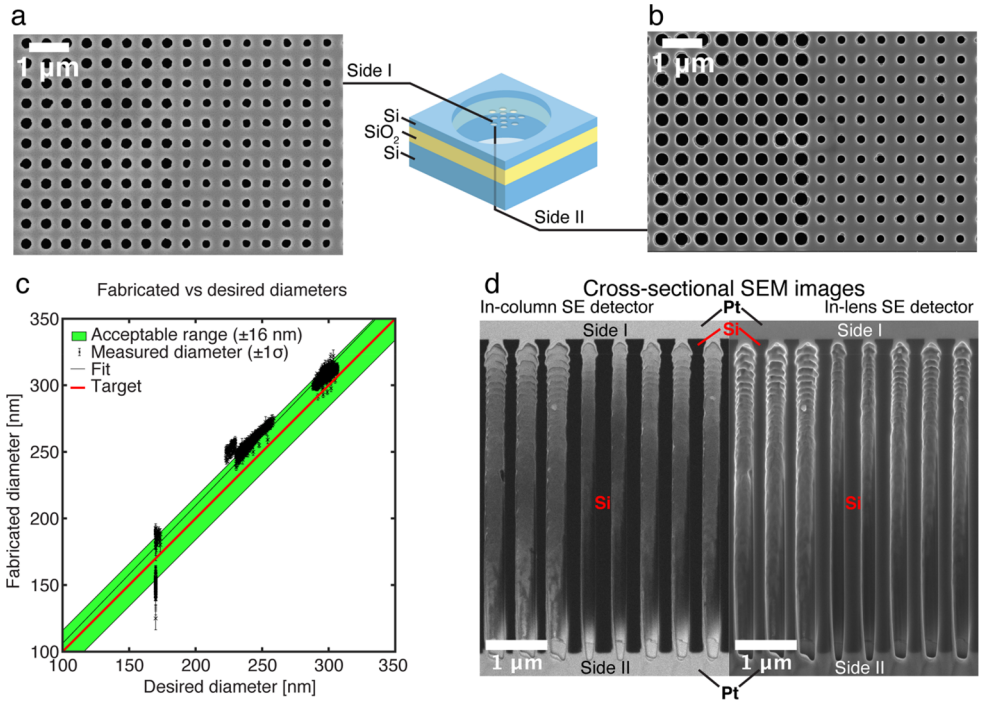

Figure 2. Holey metalens fabrication results. (a) Scanning electron microscopy (SEM) image of the holes on side I of the holey metalens. (b) SEM image of the holes on side II of the metalens. (c) Measured hole size of the fabricated lens as a function of designed hole size. The diameters were measured on side II of the fabricated lens. The diameter deviation tolerance range of ±16 nm is indicated as the shaded green area, and the error bars represent one standard deviation in measured diameters. The exposure dose used for electron beam patterning of the resist was slightly higher than desirable, producing slightly larger hole diameters than designed. (d) Cross-sectional SEM images of a separate holey metalens. The same cross-section is captured using two secondary electron (SE) detectors, an in-column detector (left), and an in-lens detector (right). Both sides of the silicon membrane are coated with platinum to increase the visual contrast between the silicon and the holes. The ridges are formed from the repeated etching and passivation cycles in the Bosch process (see Supporting Information section S3 for more details). The side I hole diameters underestimate the hole diameter through the depth due to the undercutting on side I.

outlined in Supplementary Figure 4 with further details in Supporting Information section S3. Electron beam lithography and reactive-ion etching are used to pattern a 400 nm thick SiO_2 hard mask on the device layer surface of an SOI chip with the desired holey metalens pattern. A deep Bosch process[62,63] is then used to etch high aspect ratio holes into the device layer using the hard mask, terminating at the SOI buried oxide layer. The hard mask is then removed with a buffered HF (BHF) wet etch. The chip is then flipped over to expose the Si handle layer, and a 4 mm circular opening directly opposite to the patterned metalens area is thinned through another Bosch etch process, which terminates on the other side of the buried oxide layer. Finally, the buried oxide is removed from the silicon membrane with a second BHF etch, exposing the patterned Si membrane that is supported at the edges by the rest of the SOI chip. We refer to the hard mask side of the membrane as side I and the buried oxide side as side II. SEM images of both sides are shown in Figure 2a,b, respectively, and a focused ion beam (FIB) cross section of the fabricated metalens is shown in Figure 2d. The hole taper values (i.e., tilt of the hole wall) at various sampled positions are within 1°. FIB cross sections are also employed to directly measure the membrane thickness at two positions, which yield a mean thickness of 5.0 μm. The fabricated hole diameters are plotted against the design diameters in Figure 2c, and most achieve the design diameter within the ±16 nm target fabrication tolerance.

The Si etch rate strongly decreases with nanohole diameter, and the etch rate dependence is plotted in Supplementary Figure 5. The use of via-holes through a thin membrane, as opposed to holes with only one open end, ensures that all the nanoholes can be etched to the same depth reproducibly, despite this aspect ratio-dependent etch rate affecting holes of various diameters within the design.

Optical Characterization. The metalens transmission properties are characterized using the setup in Supplementary Figure 6a with further details in Supporting Information section S4. The holey metalens is illuminated from side II by a uniform beam with the same diameter as the lens, and the transmitted light is imaged using a microscope (Figure 3a). A focal spot corresponds to the point-spread-function from a point source placed at infinity. Figure 3b shows the transverse (xy) cross sections of the experimentally measured focal spot, superimposed onto the ideal Airy disk profile. Linear cross sections yield a full width at half-maximum (fwhm) of 3.298 ± 0.009 μm, which is close to the ideal Airy fwhm of 3.285 μm for the system.

The Strehl ratio (SR), the ratio of the focal spot peak intensity to the ideal Airy disk maximum computed for the same lens aperture, is commonly employed to quantify the quality of focusing. Maréchal's criterion states that a lens can be considered diffraction limited when SR, which takes values between 0 and 1, is above 0.8.[64] We find that the fabricated device exhibits diffraction-limited behavior with SR = 0.94 ± 0.06.

Efficiency Measurements. We measure the holey metalens focusing efficiency by computing the ratio of the transmitted power contained within the focal spot to the incident power. A 20 μm diameter aperture is placed in the

https://doi.org/10.1021/acs.nanolett.1c02612
Nano Lett. 2021, 21, 8642−8649

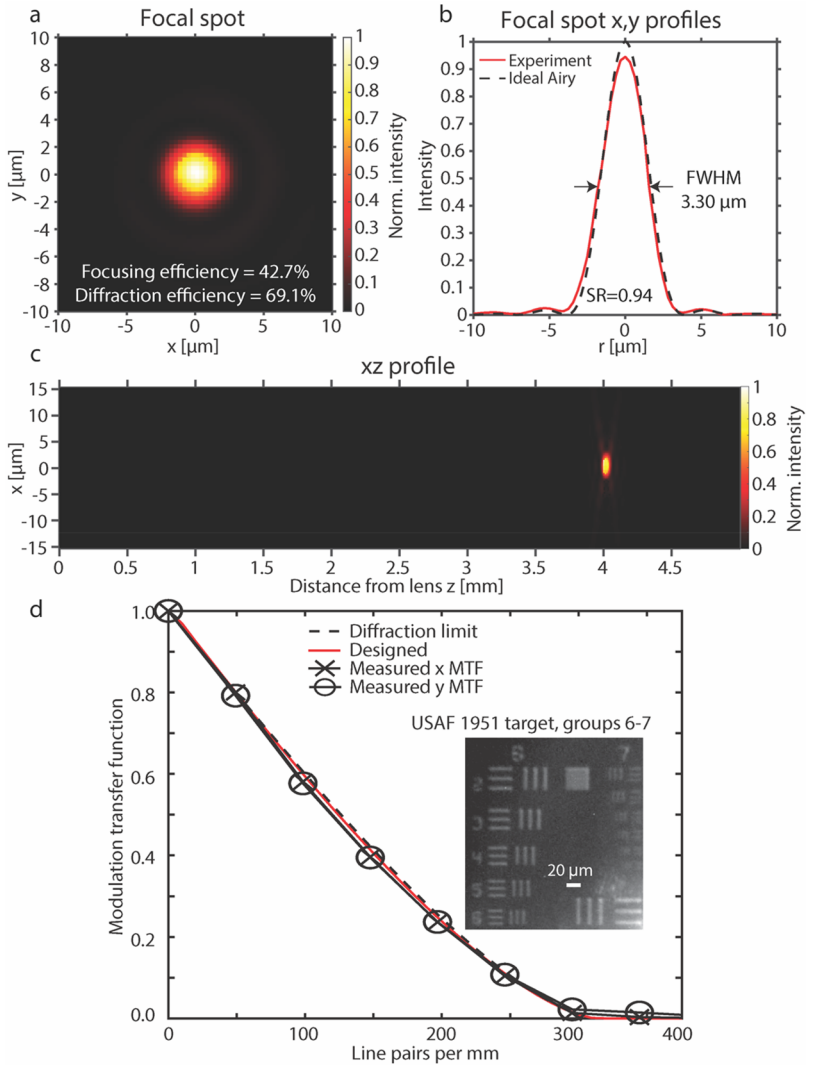

Figure 3. Optical characterization of a holey metalens. (a) Focal spot in the transverse (xy) plane at the focal distance of $f = 4$ mm. (b) Transverse cut of the experimental focal spot intensity profile (red solid line) superimposed on an ideal Airy disk profile (black dashed line). The Strehl ratio of this focal spot is 0.94 ± 0.06 and the full width at half intensity maximum (fwhm) of the spot is 3.298 ± 0.009 μm, close to the ideal Airy fwhm of 3.285 μm. (c) Longitudinal (xz) profile of the focusing profile, which shows one primary focus and no significant secondary foci. (c) Modulation transfer function (MTF) of the fabricated holey metalens (cross and circular markers) compared to simulated results (red solid line) and the diffraction limit (dashed black line). The inset shows groups 6 and 7 of USAF test object imaged through the metalens.

focal plane to block out light around the focal spot. The focal spot and incident laser power values are measured directly using a power meter (Supplementary Figure 6b). The focusing efficiency is measured to be 42.7%, which is smaller than the design value of 68.7%. When the focal spot power is normalized to the transmitted power instead (i.e., without the 20 μm aperture), we obtain the relative or diffraction efficiency of 69.1%, which is also smaller than the design value of 93.3%. The lower efficiencies compared to the design values can be primarily attributed to the device thickness of 5.0 μm deviating from the design thickness of 5.3 μm and secondarily to the slightly larger hole diameters compared to the design values (Figure 2c). Figure 3c plots the experimentally obtained longitudinal (z) scan, which shows the primary focus and no significant secondary foci.

MTF Measurements. The holey metalens imaging quality at normal incidence is equivalent to that of a diffraction-limited system, as seen by how it closely tracks the diffraction-limited modulation transfer function (MTF) for both simulated and experimental measurements (Figure 3d). The MTF captures how an optical system blurs or reduces the contrast of an incoherent periodic pattern imaged through the system as a function of the pattern spatial frequency. We obtain the MTF by Fourier transformation of the numerical and experimental point spread functions.[65] The inset of Figure 3d exhibits an image of groups 6 and 7 of the standard USAF 1951 resolution target captured through the holey metalens in the imaging setup of Supplementary Figure 6c. The constant image background was subtracted. The imaging setup can resolve up to element 2 of group 7, which corresponds to a spatial resolution of 143.7 line pairs per mm and a line width of 3.48 μm.

DISCUSSION

The large aspect ratios afforded by the holey meta-atoms expands the range of group delays $\frac{\partial\phi(r,\omega)}{\partial\omega}$, sometimes known as phase dispersion,[66] where ω is the incident light angular

https://doi.org/10.1021/acs.nanolett.1c02612
Nano Lett. 2021, 21, 8642−8649

frequency, that can be achieved as a direct result of the thicker optical path length through the meta-atoms. Ignoring cavity effects from interfacial reflections, the transmitted light phase can be approximated as $\phi(\omega,H) = \omega n_{\text{eff}} H/c$, where c is the speed of light, which allows the group delay to be written as[40]

$$\frac{\partial\phi(\omega, H)}{\partial\omega} = H\left(\frac{1}{c}n_{\text{eff}} + \frac{\omega}{c}\frac{\partial n_{\text{eff}}}{\partial\omega}\right) \tag{2}$$

The range of group delays $\left.\frac{\partial\phi(\omega,H)}{\partial\omega}\right|_{\text{max}} - \left.\frac{\partial\phi(\omega,H)}{\partial\omega}\right|_{\text{min}}$ accessible by a set of single-layer meta-atoms, which have a fixed range of effective indices, thus scales linearly with H. More precise bounds for transparent dielectric metalenses in general also show that this range scales linearly with H.[39] This is directly relevant for the development of large-area achromatic metalenses, since such devices require a spatially variant group delay in addition to the spatially variant optical phase that produces focusing. The maximum radius R of an achromatic metalens is proportional to the maximum range of group delays for the same lens NA (eq 3);[66] thus the use of ultradeep hole-like meta-atoms opens the path toward achieving centimeter-scale achromatic metasurfaces.

$$R_{\text{max}} = \left(\left.\frac{\partial\phi(\omega, H)}{\partial\omega}\right|_{\text{max}} - \left.\frac{\partial\phi(\omega, H)}{\partial\omega}\right|_{\text{min}}\right)\frac{c}{\frac{1}{\text{NA}} - \sqrt{\frac{1}{\text{NA}^2} - 1}} \tag{3}$$

It will be necessary for one to use a much wider range of shapes beyond the cylindrical geometries studied in this report to realize such an achromatic metalens because one must independently control the optical phase and group delay for each meta-atom. The cylindrical holes in this paper have group delays that are nonlinearly correlated with the transmitted phase, and achieve a range of group delays from to −13.0 to 64.6 fs (77.6 fs range) when evaluated for the wavelength range from λ = 1.4 to 1.7 μm and for the full set of diameters smaller than the 500 nm pitch, which may enable the fabrication of an achromatic metalens with a diameter of 380 μm for NA = 0.24, provided the library is expanded to increase shape variation and allow independent control of the transmitted phase and group delay. Notably, due to the substrateless configuration, such meta-atom structures must be directly connected to the membrane bulk, which necessitates "scaffolding" for material inclusions within a nanohole.

Another possible direction will be in filling these nanoholes with liquid crystals or nonlinear materials to add dynamical control to the properties of these metasurfaces. Such control has been demonstrated with liquid crystals enveloping pillar-based metasurfaces.[67−69]

The metalenses here are fabricated using entirely CMOS-compatible processes with the sole exception of electron beam lithography. However, this serial lithography step can be replaced with high throughput photolithography techniques to achieve scalable metalens manufacturing with high reproducibility using technologies deployed at existing semiconductor foundries.[70] Previous works have achieved large area pillar-based metalenses using i-line,[70] deep ultraviolet (DUV),[5] and immersion DUV lithography,[71] and these techniques can also be applied to large area holey metalenses. For applications in which the mechanical deformation of a thin membrane must be avoided, the holey metalens can be bonded to a silicon wafer substrate on side I just after the Bosch etch and hard mask removal. This will provide mechanical support and prevent the large-area membrane from sagging.

■ ASSOCIATED CONTENT

Supporting Information

The Supporting Information is available free of charge at https://pubs.acs.org/doi/10.1021/acs.nanolett.1c02612.

Additional theoretical investigation of comparison between pillar and hole meta-atoms, numerical calculation details, nanofabrication protocol, and optical characterization experimental details (PDF)

■ AUTHOR INFORMATION

Corresponding Authors

Soon Wei Daniel Lim − *Harvard John A. Paulson School of Engineering and Applied Sciences, Cambridge, Massachusetts 02138, United States;* orcid.org/0000-0003-1689-6860; Email: lim982@g.harvard.edu

Federico Capasso − *Harvard John A. Paulson School of Engineering and Applied Sciences, Cambridge, Massachusetts 02138, United States*; Email: capasso@seas.harvard.edu

Author

Maryna L. Meretska − *Harvard John A. Paulson School of Engineering and Applied Sciences, Cambridge, Massachusetts 02138, United States*

Complete contact information is available at: https://pubs.acs.org/10.1021/acs.nanolett.1c02612

Author Contributions

†S.W.D.L. and M.L.M. contributed equally to this work.

Notes

The authors declare the following competing financial interest(s): A provisional patent (US 63/106,825) based on this work is pending. The authors declare no other competing interests.

■ ACKNOWLEDGMENTS

This project is supported by the Defense Advanced Research Projects Agency (DARPA), Grant HR00111810001. S.W.D.L. is supported by A*STAR Singapore through the National Science Scholarship Scheme. M.L.M. is supported by NWO Rubicon Grant 019.173EN.010, by the Dutch Funding Agency NWO. This work was performed in part at the Harvard University Center for Nanoscale Systems (CNS), a member of the National Nanotechnology Coordinated Infrastructure Network (NNCI), which is supported by the National Science Foundation under NSF Award ECCS-2025158. The authors thank Wei Ting Chen and Joon-Suh Park for valuable discussions and No-No Groenen for providing artistic renders.

■ REFERENCES

(1) Khorasaninejad, M.; Capasso, F. Metalenses: Versatile Multifunctional Photonic Components. *Science* **2017**, *358* (6367), eaam8100.

(2) Chang, C.-C.; Zhao, Z.; Li, D.; Taylor, A. J.; Fan, S.; Chen, H.-T. Broadband Linear-to-Circular Polarization Conversion Enabled by Birefringent Off-Resonance Reflective Metasurfaces. *Phys. Rev. Lett.* **2019**, *123* (23), 237401.

(3) Alaee, R.; Vaddi, Y.; Boyd, R. W. Dynamic Coherent Perfect Absorption in Nonlinear Metasurfaces. *Opt. Lett.* **2020**, *45* (23), 6414−6417.
(4) Kwon, H.; Zheng, T.; Faraon, A. Nano-Electromechanical Tuning of Dual-Mode Resonant Dielectric Metasurfaces for Dynamic Amplitude and Phase Modulation. *Nano Lett.* **2021**, *21* (7), 2817−2823.
(5) Park, J.; Zhang, S.; She, A.; Chen, W. T.; Lin, P.; Yousef, K. M. A.; Cheng, J.; Capasso, F. All-Glass, Large Metalens at Visible Wavelength Using Deep-Ultraviolet Projection Lithography. *Nano Lett.* **2019**, *19* (12), 8673−8682.
(6) Rubin, N. A.; D'Aversa, G.; Chevalier, P.; Shi, Z.; Chen, W. T.; Capasso, F. Matrix Fourier Optics Enables a Compact Full-Stokes Polarization Camera. *Science* **2019**, *365* (6448), eaax1839.
(7) Chen, W. T.; Zhu, A. Y.; Capasso, F. Flat Optics with Dispersion-Engineered Metasurfaces. *Nature Reviews Materials* **2020**, *5* (8), 604−620.
(8) Hu, T.; Zhong, Q.; Li, N.; Dong, Y.; Xu, Z.; Fu, Y. H.; Li, D.; Bliznetsov, V.; Zhou, Y.; Lai, K. H.; Lin, Q.; Zhu, S.; Singh, N. CMOS-Compatible a-Si Metalenses on a 12-Inch Glass Wafer for Fingerprint Imaging. *Nanophotonics* **2020**, *9* (4), 823−830.
(9) Yoon, G.; Kim, K.; Huh, D.; Lee, H.; Rho, J. Single-Step Manufacturing of Hierarchical Dielectric Metalens in the Visible. *Nat. Commun.* **2020**, *11* (1), 2268.
(10) Einck, V. J.; Torfeh, M.; McClung, A.; Jung, D. E.; Mansouree, M.; Arbabi, A.; Watkins, J. J. Scalable Nanoimprint Lithography Process for Manufacturing Visible Metasurfaces Composed of High Aspect Ratio TiO2Meta-Atoms. *ACS Photonics* **2021**, *8*, 2400−2409.
(11) Yin, L.; Vlasko-Vlasov, V. K.; Pearson, J.; Hiller, J. M.; Hua, J.; Welp, U.; Brown, D. E.; Kimball, C. W. Subwavelength Focusing and Guiding of Surface Plasmons. *Nano Lett.* **2005**, *5* (7), 1399−1402.
(12) Liu, Z.; Steele, J. M.; Srituravanich, W.; Pikus, Y.; Sun, C.; Zhang, X. Focusing Surface Plasmons with a Plasmonic Lens. *Nano Lett.* **2005**, *5* (9), 1726−1729.
(13) Huang, F. M.; Zheludev, N.; Chen, Y.; Javier Garcia de Abajo, F. Focusing of Light by a Nanohole Array. *Appl. Phys. Lett.* **2007**, *90* (9), 091119.
(14) Shi, H.; Wang, C.; Du, C.; Luo, X.; Dong, X.; Gao, H. Beam Manipulating by Metallic Nano-Slits with Variant Widths. *Opt. Express* **2005**, *13* (18), 6815.
(15) Verslegers, L.; Catrysse, P. B.; Yu, Z.; White, J. S.; Barnard, E. S.; Brongersma, M. L.; Fan, S. Planar Lenses Based on Nanoscale Slit Arrays in a Metallic Film. *Nano Lett.* **2009**, *9* (1), 235−238.
(16) Kildishev, A. v.; Boltasseva, A.; Shalaev, V. M. Planar Photonics with Metasurfaces. *Science* **2013**, *339* (6125), 1232009−1232009.
(17) Khurgin, J. B.; Boltasseva, A. Reflecting upon the Losses in Plasmonics and Metamaterials. *MRS Bull.* **2012**, *37* (8), 768−779.
(18) Yang, Y.; Wang, W.; Moitra, P.; Kravchenko, I. I.; Briggs, D. P.; Valentine, J. Dielectric Meta-Reflectarray for Broadband Linear Polarization Conversion and Optical Vortex Generation. *Nano Lett.* **2014**, *14* (3), 1394−1399.
(19) Devlin, R. C.; Khorasaninejad, M.; Chen, W. T.; Oh, J.; Capasso, F. Broadband High-Efficiency Dielectric Metasurfaces for the Visible Spectrum. *Proc. Natl. Acad. Sci. U. S. A.* **2016**, *113* (38), 10473−10478.
(20) Schonbrun, E.; Seo, K.; Crozier, K. B. Reconfigurable Imaging Systems Using Elliptical Nanowires. *Nano Lett.* **2011**, *11* (10), 4299−4303.
(21) Khorasaninejad, M.; Chen, W. T.; Devlin, R. C.; Oh, J.; Zhu, A. Y.; Capasso, F. Metalenses at Visible Wavelengths: Diffraction-Limited Focusing and Subwavelength Resolution Imaging. *Science* **2016**, *352* (6290), 1190−1194.
(22) Schonbrun, E.; Seo, K.; Crozier, K. B. Reconfigurable Imaging Systems Using Elliptical Nanowires. *Nano Lett.* **2011**, *11* (10), 4299−4303.
(23) Shalaginov, M. Y.; An, S.; Zhang, Y.; Yang, F.; Su, P.; Liberman, V.; Chou, J. B.; Roberts, C. M.; Kang, M.; Rios, C.; Du, Q.; Fowler, C.; Agarwal, A.; Richardson, K. A.; Rivero-Baleine, C.; Zhang, H.; Hu, J.; Gu, T. Reconfigurable All-Dielectric Metalens with Diffraction-Limited Performance. *Nat. Commun.* **2021**, *12* (1), 1225.
(24) Chantakit, T.; Schlickriede, C.; Sain, B.; Meyer, F.; Weiss, T.; Chattham, N.; Zentgraf, T. All-Dielectric Silicon Metalens for Two-Dimensional Particle Manipulation in Optical Tweezers. *Photonics Res.* **2020**, *8* (9), 1435−1440.
(25) Balthasar Mueller, J. P.; Leosson, K.; Capasso, F. Ultracompact Metasurface In-Line Polarimeter. *Optica* **2016**, *3* (1), 42−47.
(26) Yu, N.; Genevet, P.; Kats, M. A.; Aieta, F.; Tetienne, J.-P.; Capasso, F.; Gaburro, Z. Light Propagation with Phase Discontinuities: Generalized Laws of Reflection and Refraction. *Science* **2011**, *334* (6054), 333−337.
(27) Zhan, A.; Colburn, S.; Trivedi, R.; Fryett, T. K.; Dodson, C. M.; Majumdar, A. Low-Contrast Dielectric Metasurface Optics. *ACS Photonics* **2016**, *3* (2), 209−214.
(28) Mehmood, M. Q.; Mei, S.; Hussain, S.; Huang, K.; Siew, S. Y.; Zhang, L.; Zhang, T.; Ling, X.; Liu, H.; Teng, J.; Danner, A.; Zhang, S.; Qiu, C. W. Visible-Frequency Metasurface for Structuring and Spatially Multiplexing Optical Vortices. *Adv. Mater.* **2016**, *28* (13), 2533−2539.
(29) Yang, Y.; Wang, W.; Moitra, P.; Kravchenko, I. I.; Briggs, D. P.; Valentine, J. Dielectric Meta-Reflectarray for Broadband Linear Polarization Conversion and Optical Vortex Generation. *Nano Lett.* **2014**, *14* (3), 1394−1399.
(30) Aieta, F.; Genevet, P.; Kats, M. A.; Yu, N.; Blanchard, R.; Gaburro, Z.; Capasso, F. Aberration-Free Ultrathin Flat Lenses and Axicons at Telecom Wavelengths Based on Plasmonic Metasurfaces. *Nano Lett.* **2012**, *12* (9), 4932−4936.
(31) Chen, W. T.; Khorasaninejad, M.; Zhu, A. Y.; Oh, J.; Devlin, R. C.; Zaidi, A.; Capasso, F. Generation of Wavelength-Independent Subwavelength Bessel Beams Using Metasurfaces. *Light: Sci. Appl.* **2017**, *6* (5), e16259−e16259.
(32) Cheng, Q.; Wang, J.; Ma, L.; Shen, Z.; Zhang, J.; Zheng, X.; Chen, T.; Yu, Y.; Yu, D.; He, Q.; Hu, W.; Li, T.; Zhuang, S.; Zhou, L. Achromatic Terahertz Airy Beam Generation with Dielectric Metasurfaces. *Nanophotonics* **2021**, *10* (3), 1123−1131.
(33) Lim, S. W. D.; Park, J.-S.; Meretska, M. L.; Dorrah, A. H.; Capasso, F. Engineering Phase and Polarization Singularity Sheets. *Nat. Commun.* **2021**, *12* (1), 4190.
(34) Li, L.; Liu, Z.; Ren, X.; Wang, S.; Su, V.-C.; Chen, M.-K.; Chu, C. H.; Kuo, H. Y.; Liu, B.; Zang, W.; Guo, G.; Zhang, L.; Wang, Z.; Zhu, S.; Tsai, D. P. Metalens-Array-Based High-Dimensional and Multiphoton Quantum Source. *Science* **2020**, *368* (6498), 1487−1490.
(35) Yang, W.; Xiao, S.; Song, Q.; Liu, Y.; Wu, Y.; Wang, S.; Yu, J.; Han, J.; Tsai, D.-P. All-Dielectric Metasurface for High-Performance Structural Color. *Nat. Commun.* **2020**, *11* (1), 1864.
(36) Wang, B.; Dong, F.; Li, Q. T.; Yang, D.; Sun, C.; Chen, J.; Song, Z.; Xu, L.; Chu, W.; Xiao, Y. F.; Gong, Q.; Li, Y. Visible-Frequency Dielectric Metasurfaces for Multiwavelength Achromatic and Highly Dispersive Holograms. *Nano Lett.* **2016**, *16* (8), 5235−5240.
(37) Li, L.; Jun Cui, T.; Ji, W.; Liu, S.; Ding, J.; Wan, X.; Bo Li, Y.; Jiang, M.; Qiu, C. W.; Zhang, S. Electromagnetic Reprogrammable Coding-Metasurface Holograms. *Nat. Commun.* **2017**, *8* (1), 197.
(38) Walter, F.; Li, G.; Meier, C.; Zhang, S.; Zentgraf, T. Ultrathin Nonlinear Metasurface for Optical Image Encoding. *Nano Lett.* **2017**, *17* (5), 3171−3175.
(39) Presutti, F.; Monticone, F. Focusing on Bandwidth: Achromatic Metalens Limits. *Optica* **2020**, *7* (6), 624−631.
(40) Chen, W. T.; Zhu, A. Y.; Sanjeev, V.; Khorasaninejad, M.; Shi, Z.; Lee, E.; Capasso, F. A Broadband Achromatic Metalens for Focusing and Imaging in the Visible. *Nat. Nanotechnol.* **2018**, *13* (3), 220−226.
(41) Schonbrun, E.; Seo, K.; Crozier, K. B. Reconfigurable Imaging Systems Using Elliptical Nanowires. *Nano Lett.* **2011**, *11* (10), 4299−4303.
(42) Diels, J.-C.; Rudolph, W. Femtosecond Optics. In *Ultrashort Laser Pulse Phenomena*; Elsevier, 2006; pp 61−142.

https://doi.org/10.1021/acs.nanolett.1c02612
Nano Lett. 2021, 21, 8642−8649

(43) Falcone, F.; Lopetegi, T.; Laso, M. A. G.; Baena, J. D.; Bonache, J.; Beruete, M.; Marques, R.; Martín, F.; Sorolla, M. Babinet Principle Applied to the Design of Metasurfaces and Metamaterials. *Phys. Rev. Lett.* **2004**, *93* (19), 2−5.
(44) Born, M.; Wolf, E. Elements of the Theory of Diffraction. In *Principles of Optics*; Pergamon Press, 1980; pp 370−458.
(45) Park, S.-G.; Lee, K.; Han, D.; Ahn, J.; Jeong, K.-H. Subwavelength Silicon Through-Hole Arrays as an All-Dielectric Broadband Terahertz Gradient Index Metamaterial. *Appl. Phys. Lett.* **2014**, *105* (9), 091101.
(46) Ong, J. R.; Chu, H. S.; Chen, V. H.; Zhu, A. Y.; Genevet, P. Freestanding Dielectric Nanohole Array Metasurface for Mid-Infrared Wavelength Applications. *Opt. Lett.* **2017**, *42* (13), 2639−2642.
(47) Wang, S.; Wu, P. C.; Su, V. C.; Lai, Y. C.; Chen, M. K.; Kuo, H. Y.; Chen, B. H.; Chen, Y. H.; Huang, T. T.; Wang, J. H.; Lin, R. M.; Kuan, C. H.; Li, T.; Wang, Z.; Zhu, S.; Tsai, D. P. A Broadband Achromatic Metalens in the Visible. *Nat. Nanotechnol.* **2018**, *13* (3), 227−232.
(48) Wang, L.; Nichelatti, A.; Schellevis, H.; de Boer, C.; Visser, C.; Nguyen, T. N.; Sarro, P. M. High Aspect Ratio Through-Wafer Interconnections for 3D-Microsystems. *Proceedings of the IEEE Micro Electro Mechanical Systems (MEMS)* **2003**, 634−637.
(49) Elam, J. W.; Routkevitch, D.; Mardilovich, P. P.; George, S. M. Conformal Coating on Ultrahigh-Aspect-Ratio Nanopores of Anodic Alumina by Atomic Layer Deposition. *Chem. Mater.* **2003**, *15* (18), 3507−3517.
(50) Groever, B.; Chen, W. T.; Capasso, F. Meta-Lens Doublet in the Visible Region. *Nano Lett.* **2017**, *17* (8), 4902−4907.
(51) Simovski, C. R. Material Parameters of Metamaterials (a Review). *Opt. Spectrosc.* **2009**, *107* (5), 726−753.
(52) Lalanne, P.; Lemercier-lalanne, D. On the Effective Medium Theory of Subwavelength Periodic Structures. *J. Mod. Opt.* **1996**, *43* (10), 2063−2085.
(53) Krokhin, A. A.; Halevi, P.; Arriaga, J. Long-Wavelength Limit (Homogenization) for Two-Dimensional Photonic Crystals. *Phys. Rev. B: Condens. Matter Mater. Phys.* **2002**, *65* (11), 115208.
(54) Lalanne, P.; Astilean, S.; Chavel, P.; Cambril, E.; Launois, H. Design and Fabrication of Blazed Binary Diffractive Elements with Sampling Periods Smaller than the Structural Cutoff. *J. Opt. Soc. Am. A* **1999**, *16* (5), 1143.
(55) Pestourie, R.; Pérez-Arancibia, C.; Lin, Z.; Shin, W.; Capasso, F.; Johnson, S. G. Inverse Design of Large-Area Metasurfaces. *Opt. Express* **2018**, *26* (26), 33732−33747.
(56) Byrnes, S. J.; Lenef, A.; Aieta, F.; Capasso, F. Designing Large, High-Efficiency, High-Numerical-Aperture, Transmissive Meta-Lenses for Visible Light. *Opt. Express* **2016**, *24* (5), 5110−5124.
(57) Marathay, A. S.; McCalmont, J. F. Vector Diffraction Theory for Electromagnetic Waves. *J. Opt. Soc. Am. A* **2001**, *18* (10), 2585−2593.
(58) Griewank, A. On Automatic Differentiation. In *Mathematical Programming: Recent Developments and Applications*; Kluwer Academic, 1989; pp 83−108.
(59) Abadi, M.; Barham, P.; Chen, J.; Chen, Z.; Davis, A.; Dean, J.; Devin, M.; Ghemawat, S.; Irving, G.; Isard, M.; Kudlur, M.; Levenberg, J.; Monga, R.; Moore, S.; Murray, D. G.; Steiner, B.; Tucker, P.; Vasudevan, V.; Warden, P.; Wicke, M.; Yu, Y.; Zheng, X. TensorFlow: A System for Large-Scale Machine Learning. *Proceedings of the 12th USENIX Symposium on Operating Systems Design and Implementation (OSDI '16)*; USENIX, 2016; pp 265−283.
(60) Campbell, S. D.; Sell, D.; Jenkins, R. P.; Whiting, E. B.; Fan, J. A.; Werner, D. H. Review of Numerical Optimization Techniques for Meta-Device Design [Invited]. *Opt. Mater. Express* **2019**, *9* (4), 1842.
(61) Young, I. T.; Zagers, R.; van Vliet, L. J.; Mullikin, J.; Boddeke, F.; Netten, H. Depth-of-Focus in Microscopy. *SCIA'93, Proceedings of the 8th Scandinavian Conference on Image Analysis*, Tromso, Norway; Norwegian Society for Image Processsing and Pattern Recognition, 1993; pp 493−498.
(62) Laermer, F.; Schilp, A. Method for Anisotropic Etching of Silicon. U.S. Patent 6,531,068 B2, 2003; Robert Bosch GmbH.
(63) Laermer, F.; Schilp, A.; Method of Anisotropically Etching Silicon. U.S. Patent 5,501,893, 1996; Robert Bosch GmbH.
(64) Maréchal, A. Etude Des Effets Combinés de La Diffraction et Des Aberrations Géométriques Sur l'image d'un Point Lumineux. *Rev. Opt., Theor. Instrum.* **1947**, *26*, 257−277.
(65) Goodman, J. W. Frequency Analysis of Optical Imaging Systems. In *Introduction to Fourier Optics*; Roberts and Company Publishers: Englewood, 2004; pp 127−172.
(66) Shrestha, S.; Overvig, A. C.; Lu, M.; Stein, A.; Yu, N. Broadband Achromatic Dielectric Metalenses. *Light: Sci. Appl.* **2018**, *7* (1), 85.
(67) Dolan, J. A.; Cai, H.; Delalande, L.; Li, X.; Martinson, A. B. F.; de Pablo, J. J.; Lopez, D.; Nealey, P. F. Broadband Liquid Crystal Tunable Metasurfaces in the Visible: Liquid Crystal Inhomogeneities Across the Metasurface Parameter Space. *ACS Photonics* **2021**, *8* (2), 567−575.
(68) Bosch, M.; Shcherbakov, M. R.; Won, K.; Lee, H.-S.; Kim, Y.; Shvets, G. Electrically Actuated Varifocal Lens Based on Liquid-Crystal-Embedded Dielectric Metasurfaces. *Nano Lett.* **2021**, *21* (9), 3849−3856.
(69) Lininger, A.; Zhu, A. Y.; Park, J. S.; Palermo, G.; Chatterjee, S.; Boyd, J.; Capasso, F.; Strangi, G. Optical Properties of Metasurfaces Infiltrated with Liquid Crystals. *Proc. Natl. Acad. Sci. U. S. A.* **2020**, *117* (34), 20390−20396.
(70) She, A.; Zhang, S.; Shian, S.; Clarke, D. R.; Capasso, F. Large Area Metalenses: Design, Characterization, and Mass Manufacturing. *Opt. Express* **2018**, *26* (2), 1573−1585.
(71) Hu, T.; Zhong, Q.; Li, N.; Dong, Y.; Xu, Z.; Fu, Y. H.; Li, D.; Bliznetsov, V.; Zhou, Y.; Lai, K. H.; Lin, Q.; Zhu, S.; Singh, N. CMOS-Compatible a-Si Metalenses on a 12-Inch Glass Wafer for Fingerprint Imaging. *Nanophotonics* **2020**, *9* (4), 823−830.

https://doi.org/10.1021/acs.nanolett.1c02612
Nano Lett. 2021, 21, 8642−8649